

Cite this: *Nanoscale*, 2011, **3**, 1861

www.rsc.org/nanoscale

PAPER

A general procedure to synthesize highly crystalline metal oxide and mixed oxide nanocrystals in aqueous medium and photocatalytic activity of metal/oxide nanohybrids†

Thanh-Dinh Nguyen, Cao-Thang Dinh and Trong-On Do*

Received 27th January 2011, Accepted 1st February 2011

DOI: 10.1039/c1nr10109a

A conventional and general route has been exploited to the high yield synthesis of many kinds of highly crystalline metal oxide and mixed oxide nanocrystals with different morphologies including belt, rod, truncated-octahedron, cubic, sphere, sheet *via* the hydrothermal reaction of inorganic precursors in aqueous solution in the presence of bifunctional 6-aminohexanoic acid (AHA) molecules as a capping agent. This method is a simple, reproducible and general route for the preparation of a variety of high-crystalline inorganic nanocrystals in scale-up. The shape of inorganic nanocrystals such as CoWO₄, La₂(MoO₄)₃ can be controlled by simply adjusting the synthesis conditions including pH solution and reaction temperature. Further, by tuning precursor monomer concentration, the mesocrystal hierarchical aggregated microspheres (*e.g.*, MnWO₄, La₂(MoO₄)₃) can be achieved, due to the spontaneous assembly of individual AHA-capped nanoparticles. These obtained AHA-capped nanocrystals are excellent supports for the synthesis of a variety of hybrid metal/oxide nanocrystals in which noble metal particles are uniformly deposited on the surface of each individual nanosupport. The photocatalytic activity of Ag/TiO₂ nanobelts as a typical hybrid photocatalyst sample for Methylene Blue degradation was also studied.

1. Introduction

Metal oxide, mixed oxide, and hybrid noble-metal/oxide nanocrystals (NCs) have great potential for electronic, magnetic, optical, and photocatalytic applications.^{1–3} Mixed oxide system composed of two or more different components has attracted particular interest because their unique properties are not usually attainable in single components.⁴ Metals highly dispersed on nanosupport surfaces show active catalysts for a variety of reactions. The origins of their high catalytic activity have been proposed to originate from one or more of three contributions: (i) presence of low coordinative metal sites; (ii) charge transfer between the support and the metal; (iii) quantum size effect.⁵ For example, the metal–semiconductor (TiO₂) interface can promote effective charge carrier transfers to favor charge separation under band gap excitation and subsequently high photo-catalytic performance.⁶ Noble metals deposited on the NC surface act as sinks for transferring the photoexcited electron from semiconductor surface to reagents to perform the oxidation.⁷ Therefore, the charge distribution between semiconductor and

metal plays an important role in the photocatalytic process. Even though a large number of studies have been reported in the literature, the key factors for improved performance in metal/oxide nanocomposites are yet to be fully understood. Thus, the development of a general approach for the fabrication of a variety of new types of metal/oxide nanohybrids is a great challenge.

Numerous methods have been documented in the recent reviews for the synthesis of a broad range of metal oxide and mixed oxide NCs.^{8–10} For example, Li *et al.*¹¹ reported a new route for the synthesis of different types of nanocrystals including magnetic/dielectric, semiconducting, rare earth fluorescent nanoparticles, which is based on a phase transfer and separation mechanism at the liquid–liquid interface, through the liquid–solid–solution process. Ying *et al.*¹² reported a protocol to transfer metal ions from an aqueous solution to an organic medium and their application in the synthesis of nanocrystals in organic solvent. Recently, our group reported the general two-phase routes for the synthesis of two classes of monodisperse metal oxide nanocrystals: rare earth oxides and transition metal oxides, using metal salts as starting precursors instead of expensive organometallic compounds.¹³ With the same synthetic protocol, we have successfully synthesized multicomponent nanocrystals with controlled size and shape, such as doughnut- and sphere-shaped LaCO₃OH nanocrystals and cerium doped LaCO₃OH.¹⁴ The shape-controlled vanadium oxide and rare

Department of Chemical Engineering, Laval University, Quebec, G1K 7P4, Canada. E-mail: Trong-On.Do@gch.ulaval.ca; Fax: +1 (418) 656 5993; Tel: +1 (418) 656 3774

† Electronic supplementary information (ESI) available: Additional TEM, XRD, XPS, FTIR, UV-vis and photoluminescence results of the nanocrystals. See DOI: 10.1039/c1nr10109a

earth orthovanadate nanocrystals using pre-prepared metal–ligand complexes were also obtained *via* a surfactant-mediated solvothermal process.^{15–17}

It is well-known that the morphology of target nanocrystals can be controlled by capping agents through kinetic and thermodynamic regulations of nuclei growth.¹⁸ Using conventional surfactants, such as fatty acids, aliphatic amines, alkyl thiols, alkyl phosphine oxides, the resulting surfactant-capped NC products are usually hydrophobic and separated in water solution. This may not be compatible for practical applications as compared to hydrophilic ones, in which water is used as reaction medium. Recently, amphiphilic amino acid biomolecules have received great attention to synthesize the water-dispersible nanocrystals in aqueous medium. The formed products can be compatible for biotechnology, due to their hydrophilic surface character.¹⁹ For example, Xu *et al.*²⁰ synthesized the amino acid-capped Au nanochains by reducing aqueous AuCl_4^- with NaBH_4 in the presence of the amino acid (glutamic acid and histidine) as a capping agent. The interaction between hydrophilic-surfaced groups ($-\text{COOH}$ and $-\text{NH}_2$) could result in the oriented-attachment process for the formation of Au nanochains from 10 to 15 nm nanospheres. Peptide-capped gold nanospheres with ~ 10 nm in diameter were recently synthesized by Aizawa *et al.*²¹ Several approaches for the controllable synthesis of titania nanocrystals and erbia micro-/nanostructures in water/ethanol media have been developed by our research group.^{22,23} Very recently, we used bifunctional 6-aminohexanoic acid as a capping agent to the controlled shape of MnWO_4 nanoparticles and their self-assembled microspheres in water medium.²⁴ For this purpose, we extend this protocol for the synthesis of a variety of highly crystalline metal oxide and mixed oxide nanocrystals with various morphologies and high yield.

On the other hand, heterogeneous photocatalysis is an economically alternative and environmentally safe technology of advanced oxidation processes for removal of organic contaminants and bacterial detoxification from water.²⁵ Photocatalytic nanoscale systems used to date were based mostly on noble metal-deposited oxide semiconductor hybrid nanocrystals and were usually operational under UV illumination.²⁶ Due to large band-gap oxide semiconductors such as titania and transition metal tungstate, metal islands deposited on the support structures serve to promote charge separation and also exhibit charge retention. Moreover, the precise control of metal cluster size, well dispersion, and composition of metal deposited on support is deemed as an essential and powerful knob to turn their band gaps, which determine the photocatalytic characteristic of this system.^{27,28} Especially, as the sizes of Au particles fall about 3 nm, the composites display exceptional catalytic behavior.²⁸ Two main routes have typically been used for the growth of such oxide hybrids. The first route employed light-induced growth of the metal onto the pre-synthesized oxide nanocrystals, as recently illustrated by our group.^{22,29} This synthetic method allows us not only to control the population of uniform metal clusters on each individual TiO_2 surface but also to control their particle size. The resulting hybrid materials exhibit much higher catalytic performance compared to that of commercial catalysts. The second route is *via* the reduced solution reaction of metal salt on the oxide nanocrystals. Available examples by these two processes include $\text{Au}@\text{CdS}$ nanorods³⁰ and $\text{Ag}@\text{Pt}$ nanorods.³¹

In this article, we report a convenient and general route for the aqueous-phase synthesis of highly crystalline metal oxide and mixed oxide nanoparticles *via* bifunctional surfactant-assisted hydrothermal process. The synthesis is based on the crystallization of inorganic precursors in water medium in the presence of 6-aminohexanoic acid. The role of 6-aminohexanoic acid biomolecule is as a chelating agent to control the morphology and to stabilize the formed nanocrystals in water medium because of their hydrophilic surface. The deposition of small noble-metal on the oxide nanocrystals was performed in water medium using metal salt and NaBH_4 as metal source and reducing agent, respectively. The optical property and photocatalytic activity of the representative metal nanodots/semiconductor oxide (Ag/TiO_2) hybrid nanocrystals were studied.

2. Experimental section

Chemicals

All chemicals were used as received without further purification. Indium nitrate hydrate ($\text{In}(\text{NO}_3)_3 \cdot x\text{H}_2\text{O}$, 99.99%), anhydrous zirconium(IV) chloride (ZrCl_4 , 99.99%), commercial titanium oxide powder (TiO_2 , 99.8%), cobalt nitrate hexahydrate ($\text{Co}(\text{NO}_3)_2 \cdot 6\text{H}_2\text{O}$, 98%), manganese nitrate tetrahydrate ($\text{Mn}(\text{NO}_3)_2 \cdot 4\text{H}_2\text{O}$, 99%), zincate nitrate hexahydrate ($\text{Zn}(\text{NO}_3)_2 \cdot 6\text{H}_2\text{O}$, 99.9%), cadmium nitrate hexahydrate ($\text{Cd}(\text{NO}_3)_2 \cdot 6\text{H}_2\text{O}$, 99.9%), lanthanum nitrate hexahydrate ($\text{La}(\text{NO}_3)_3 \cdot 6\text{H}_2\text{O}$, 99.9%), neodymium nitrate hexahydrate ($\text{Nd}(\text{NO}_3)_3 \cdot 6\text{H}_2\text{O}$, 99.9%), yttrium nitrate hexahydrate ($\text{Y}(\text{NO}_3)_3 \cdot 6\text{H}_2\text{O}$, 99.9%), cerium nitrate hexahydrate ($\text{Ce}(\text{NO}_3)_3 \cdot 6\text{H}_2\text{O}$, 99.9%), samarium nitrate hexahydrate ($\text{Sm}(\text{NO}_3)_3 \cdot 6\text{H}_2\text{O}$, 99.9%), gadolinium nitrate hexahydrate ($\text{Gd}(\text{NO}_3)_3 \cdot 6\text{H}_2\text{O}$, 99.9%), erbium nitrate hydrate ($\text{Er}(\text{NO}_3)_3 \cdot x\text{H}_2\text{O}$, 99.9%), sodium tungstate dihydrate ($\text{Na}_2\text{WO}_4 \cdot 2\text{H}_2\text{O}$, 99.9%), vanadium pentoxide (V_2O_5 , 99.6%), silver nitrate (AgNO_3), chlorauric acid ($\text{HAuCl}_4 \cdot 3\text{H}_2\text{O}$), 6-aminohexanoic acid ($\text{HOCC}_5\text{H}_{10}\text{NH}_2$, or AHA, tech. grade, 70%), sodium borohydride (NaBH_4) were purchased from Sigma-Aldrich. Sodium hydroxide and anhydrous ethanol were purchased from Reagent ACS.

Synthesis of metal oxide NCs (In_2O_3 , Y_2O_3 , ZrO_2 , TiO_2 , CeO_2)

Metal oxide NCs were prepared by a standard alkali hydrothermal treatment process. In a typical synthesis, 0.03 mol of each inorganic precursor ($\text{In}(\text{NO}_3)_3$, $\text{Y}(\text{NO}_3)_3$, ZrCl_4 , commercial TiO_2 powder, $\text{Ce}(\text{NO}_3)_3$) was poured to 6-aminohexanoic acid aqueous solution (10 mL, 1.5 M) under stirring and then a NaOH solution (15 M, 20 mL) was poured. The pH value of the initial solution was ~ 12 . The resulting reaction mixture (30 mL) was transferred to a 50 mL Teflon-lined stainless steel autoclave and treated to 180°C for 20 h, and subsequently to cool naturally to room temperature. The obtained products were filtered out and washed by distilled water for several times to remove impurities, and dried at 60°C for 2 h.

Synthesis of mixed metal oxide NCs (tungstate, vanadate, molybdate)

(i) Vanadate and molybdate precursors were prepared from bulk V_2O_5 and bulk MoO_3 powders, respectively. Typically, bulk

V₂O₅ powder (0.30 mmol, 0.055 g) and NaOH solution (20 mL, 0.09 M) were mixed for the formation of 0.03 M Na₃VO₄ solution; bulk MoO₃ powders (0.92 mmol, 0.13 g) and NaOH solution (20 mL, 0.09 M) were mixed for the formation of 0.045 M Na₂MoO₄ solution at room temperature under magnetic stirring for about 30 min. (ii) For the synthesis of mixed metal oxide NCs, metal nitrates (0.61 mmol), 6-aminohexanoic acid (1.22 mmol, 0.16 g), were dissolved in 20 mL distilled water. An aqueous 0.03 M sodium tungstate, 0.03 M vanadate, or 0.045 M molybdate solution (20 mL) was dissolved in the above solution under stirring for 10 min at room temperature. An amorphous precipitate was generated immediately from the combination of metal cation and tungstate/vanadate/molybdate anion. The pH value of the initial solution was ~8. The resulting reaction mixture (40 mL) was transferred to a 70 mL Teflon-lined stainless steel autoclave and treated to 180 °C for 20 h. The obtained products were filtered out and washed by distilled water, and dried at 60 °C for 2 h.

Synthesis of metal (Ag, Au)/oxide hybrid NCs

AgNO₃ or HAuCl₄ aqueous solution (5 mL, 3.82–11.45 mM) was injected into 5 mL of an aqueous oxide suspension (0.2 g for each of the pre-synthesized CeO₂, TiO₂, In₂O₃, Y₂O₃, CoWO₄, MnWO₄, La₂(MoO₄)₃ NC powders) under stirring. Ag or Au ion precursors were adsorbed on the hydrophilic surface of oxide semiconductor nanocrystals and were then reduced to zerovalent metal particles by injecting 10 mL of 0.019 M NaBH₄ aqueous solution. The pH value of the reaction solution was ~7. The whole loading amount of metal in synthesis solution was changed from 5.0 to 15.0 weight percent. The reaction mixture (20 mL) was then stirred vigorously and placed in a 30 °C water bath. Within 4 h, the color of the reaction solution changed to gray for Ag and to light pink for Au, indicating the formation of the deposited metallic Ag and Au particles, respectively. A precipitated powder was collected and washed by distilled water for several times to remove impurities. The sample was further dried at 60 °C for 2 h.

Characterization

X-ray diffraction (XRD) patterns were recorded on a Bruker SMART APEXII X-ray diffractometer, using Cu K_α radiation ($\lambda = 1.5418 \text{ \AA}$). Scanning electron microscope (SEM) images of products were obtained from a JEOL 6360 instrument working at 3 kV. Transmission electron microscope (TEM) images and selected area electron diffraction (SAED) of the samples were obtained on a JEOL JEM 1230 operated at 120 kV. Samples were prepared by placing a drop of a dilute anhydrous ethanol dispersion of crystals onto a 200 mesh carbon-coated copper grid and immediately evaporated at ambient temperature. XPS measurements were carried out in an ion-pumped chamber (evacuated to 10⁻⁹ Torr) of a photoelectron spectrometer (Kratos Axis-Ultra) equipped with a focused X-ray source (Al K_α, $h\nu = 1486.6 \text{ eV}$). The binding energy of the samples was calibrated by setting the C 1 s peak to 285 eV. The peaks were deconvoluted by means of a standard CasaXPS software (v.2.3.13; product of CasaXPS Software Ltd., USA) to resolve the separate constituents after background subtraction.

UV-visible spectra of the nanohybrids were recorded for the powder sample on a Cary 300 Bio UV-visible spectrophotometer using MgO as reference.

Photocatalytic activities of the samples were evaluated by the photocatalytic decolorization of Methylene Blue (MB) under UV-visible irradiation using a 100 W Hg lamp. In each experiment, 0.015 g of catalyst was added to 16 mL of MB solution (0.03 mM). Before illumination, the suspension was magnetically stirred in the dark for 30 min to ensure the establishment of an adsorption–desorption equilibrium between the catalyst and MB. The solution was then exposed to UV-visible light irradiation under magnetic stirring. At given time intervals (80 min), 16 mL of suspension was sampled and centrifuged to remove the photocatalyst particles. The UV-vis adsorption spectrum of the centrifuged solution was then recorded using a Cary 300 Bio UV-visible spectrophotometer. The photocatalytic activity of TiO₂ samples was calculated from the absorbance peak area [$\ln(A)$]. Nearly exact ($R^2 \approx 1$) logarithmic linearity was found between the MB absorbance and the UV exposure time.

3. Results and discussion

The synthetic conditions, crystalline phases, and morphologies of a variety of metal oxide and mixed metal oxide nanocrystals are summarized in Table 1. The metal oxide and metal mixed oxide nanocrystals (NCs) were formed from the hydrothermal crystallization in an aqueous solution containing inorganic precursor and 6-aminohexanoic acid (AHA) at 180 °C for 20 h. These obtained nanocrystals were capped by –NH₂ heads of bifunctional AHA molecules and free –COOH groups of other end of AHA molecules were available for further derivatization in polar solvent.²⁴ Furthermore, noble metal highly dispersed on the oxide NC surface was also prepared *via* the controllable deposition of noble-metal precursors on the hydrophilic surface of these oxide NCs. The role of capping 6-aminohexanoic acid is to capture metal ion by its interaction with –COOH group, which favors for the formation of highly dispersed metal on the oxide surface during the synthesis. This synthetic procedure is simple, high yield, and large-scale production, so that it may be a green process and convenient to transfer to industrial application. Scheme 1 represents a general route for the high-yield synthesis and highly crystalline metal oxide and mixed oxide NCs as well as noble-metal dispersed oxide hybrid nanocrystals with different morphologies.

Metal oxides including In₂O₃, Y₂O₃, ZrO₂, TiO₂, CeO₂ were selected to illustrate our approach (Scheme 1A) because they are widely recognized for their unique properties as supports and catalysts. Metal oxide NCs were obtained by hydrolysis of the corresponding metal nitrate or bulk oxide powder in basic solution (pH \approx 12) in the presence of 6-aminohexanoic acid ligand. Under the hydrothermal treatment, metal ions were hydrolyzed to form metal hydroxide and then dehydrated to metal oxide, which further condenses into primary oxide clusters. These clusters aggregated to produce the nuclei, subsequently the oxide nanocrystals were formed *via* further growth of these nuclei. As seen in Fig. 1, XRD patterns of the resulting samples are well-matched to cubic In₂O₃ (JCPDS 006-0416), monoclinic Y₂O₃ (JCPDS 44-0399), monoclinic ZrO₂ (JCPDS 37-1484),

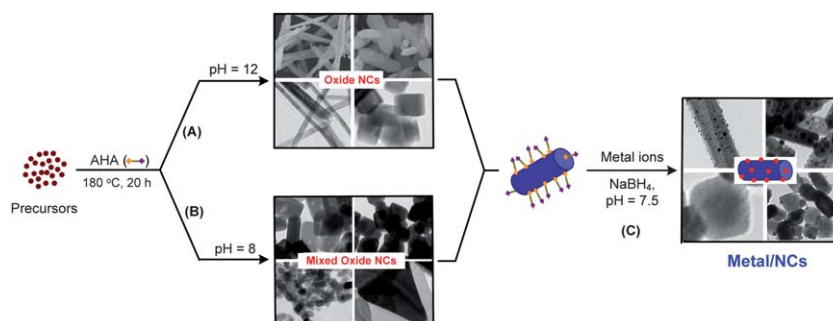
Table 1 Synthesis conditions, structures, and morphologies of a variety of high-crystalline metal oxide and metal mixed oxide nanocrystals *via* 6-aminohexanoic acid-assisted hydrothermal process^a

Sample	Inorganic precursor	Yield (%)	Solvent	Product	Structure	Shape	Size/nm
Metal oxide NCs							
1	In ³⁺	93	Basic medium	In ₂ O ₃	Cubic	Rod	80 × 6000
2	Y ³⁺	93	Basic medium	Y ₂ O ₃	Monoclinic	Rod	80 × 6000
3	Zr ⁴⁺	93	Basic medium	ZrO ₂	Monoclinic	Rod	0.5 × 1000
4	Ti ⁴⁺	93	Basic medium	TiO ₂	Brookite	Belt	60 × 8000
5	Ce ³⁺	93	Basic medium	CeO ₂	Cubic	Cubic	50
Transition metal tungstate NCs							
6	Co ²⁺ , WO ₄ ²⁻	96	Water	CoWO ₄	Monoclinic	Truncated octahedral	40
7	Mn ²⁺ , WO ₄ ²⁻	96	Water	MnWO ₄	Monoclinic	Rod	25 × 50
8	Zn ²⁺ , WO ₄ ²⁻	96	Water	ZnWO ₄	Monoclinic	Rod	15 × 70
9	Cd ²⁺ , WO ₄ ²⁻	96	Water	CdWO ₄	Monoclinic	Rod	50 × 160
Rare earth orthovanadate NCs							
10	La ³⁺ , VO ₄ ³⁻	96	Water	LaVO ₄	Monazite	Rod	8 × 40
11	Ce ³⁺ , VO ₄ ³⁻	96	Water	CeVO ₄	Tetragonal	Rod	10 × 30
12	Nd ³⁺ , VO ₄ ³⁻	96	Water	NdVO ₄	Tetragonal	Rod	10 × 35
13	Sm ³⁺ , VO ₄ ³⁻	96	Water	SmVO ₄	Tetragonal	Cubic	30
14	Gd ³⁺ , VO ₄ ³⁻	96	Water	GdVO ₄	Tetragonal	Quasi-sphere	30
15	Er ³⁺ , VO ₄ ³⁻	96	Water	ErVO ₄	Tetragonal	Sphere	30
Rare earth molybdate NCs							
16	La ³⁺ , MoO ₄ ²⁻	96	Water	La ₂ (MoO ₄) ₃	Tetragonal	Sheet	2 × 200–300
17	Ce ³⁺ , MoO ₄ ²⁻	96	Water	Ce ₂ (MoO ₄) ₃	Tetragonal	Sheet	2 × 200–300
18	Gd ³⁺ , MoO ₄ ²⁻	96	Water	Gd ₂ (MoO ₄) ₃	Tetragonal	Sheet	2 × 200–300
19	Y ³⁺ , MoO ₄ ²⁻	96	Water	Y ₂ (MoO ₄) ₃	Tetragonal	Sheet	2 × 200–300
20	Er ³⁺ , MoO ₄ ²⁻	96	Water	Er ₂ (MoO ₄) ₃	Tetragonal	Sheet	2 × 200–300

^a All samples were hydrothermally synthesized using 6-aminohexanoic acid as a capping agent at 180 °C for 20 h.

pure brookite TiO₂ (JCPDS 291-361) without mixture of rutile or anatase phase, and cubic CeO₂ (JCPDS 34-0394). The broadening and well-resolved diffraction peaks can be attributed to the nanoscale nature and high crystallinity of the samples; no peaks of any other phases or impurities were detected. Fig. 2 shows representative SEM/TEM images of the nanocrystalline samples of In₂O₃, Y₂O₃, ZrO₂, TiO₂, CeO₂. The In₂O₃ and Y₂O₃ NCs both exhibit a long rod shape with an average diameter of 80 nm and length of 6 μm (Fig. 2a–d), while the ZrO₂ sample shows short nanorod with an average diameter of 0.5 μm and length of 1 μm (Fig. 2e and f). TiO₂ nanocrystals with high aspect ratio (60 nm × 8 μm) were mostly belt-like shape (Fig. 2g and h). Unlike the rod morphology of above oxides, the product CeO₂ is mainly composed of ultrafine nanocubes with a mean edge length of 50 nm (Fig. 2l). These hydrophilic-surfaced oxide nanocrystals with high crystallinity could be used as an interesting support for the fabrication of novel metal-dispersed oxide hybrid nanocrystals with improved catalytic performance.

The procedure (Scheme 1A) was further used to synthesize mixed metal oxide nanocrystals such as mixed metal tungstates, orthovanadates, and molybdates. Three types of these mixed oxide materials have been the subjects of extensive research in recent years due to their potential applications in various fields.^{32–34} For example, metal tungstates are a good photocatalyst for the degradation of organic compounds under UV irradiation in order to purify wastewater from households and industries;³⁵ rare earth molybdates are a promising candidate in laser hosts and up-conversion lasing application.³⁶ Rare earth vanadates are highly active and selective catalysts for many organic reactions including oxidative dehydrogenation of alkanes/olefins.³⁷ However, the synthesis of these materials with hydrophilic surface still remains a challenge. For this purpose, we developed a simple method for the synthesis of these hydrophilic-surfaced nanocrystals *via* the hydrothermal reaction of an aqueous mixture containing corresponding metal cation (transition metal, rare earth) and anion (WO₄²⁻, VO₄³⁻, MoO₄²⁻)



Scheme 1 A general procedure to synthesize highly crystalline metal oxide, mixed oxide, and hybrid metal/oxide nanocrystals in aqueous medium.

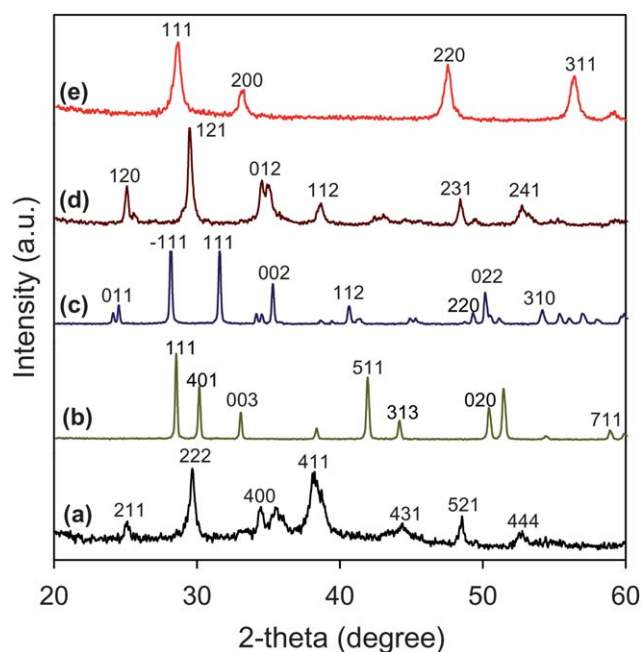


Fig. 1 XRD patterns of the as-synthesized metal oxide NC samples: (a) In_2O_3 , (b) Y_2O_3 , (c) ZrO_2 , (d) TiO_2 , and (e) CeO_2 .

in the presence of 6-aminohexanoic acid ligand (Scheme 1B). XRD patterns of the as-synthesized transition-metal tungstate NC samples are shown in Fig. 3. The diffraction peaks of all

samples are well-indexed to pure monoclinic structure: CoWO_4 ($a = 4.947 \text{ \AA}$, $b = 5.682 \text{ \AA}$, $c = 4.669 \text{ \AA}$, JCPDS 30-0443), MnWO_4 ($a = 4.80 \text{ \AA}$, $b = 5.71 \text{ \AA}$, $c = 4.97 \text{ \AA}$, JCPDS 80-0134), ZnWO_4 ($a = 4.689 \text{ \AA}$, $b = 5.724 \text{ \AA}$, $c = 4.923 \text{ \AA}$, JCPDS 15-0774), and CdWO_4 ($a = 5.026 \text{ \AA}$, $b = 5.078 \text{ \AA}$, $c = 5.867 \text{ \AA}$, JCPDS 14-676). The XRD patterns show broadening and intensive diffraction peaks due to their nanometre size and high crystallinity. No other XRD peaks for impurities were observed.

Representative TEM images of CoWO_4 , MnWO_4 , ZnWO_4 , CdWO_4 nanocrystals are shown in Fig. 4. Under the same synthesis conditions ($\text{pH} \approx 9$, $180 \text{ }^\circ\text{C}$, 20 h), the CoWO_4 nanocrystals mainly display truncated octahedron-like shape with uniform size distribution (Fig. 4a). A single truncated octahedron is $\sim 40 \text{ nm}$ in size as measured along the longest edge. The surface of the truncated octahedral nanocrystals is smooth with no obvious defects. In order to study the effect of pH of the synthesis solution on shape of the resulting CoWO_4 nanocrystals, one series of experiments was carried out with different pH values in the synthetic solution. The pH value in the initial solution was adjusted by using 1 M NaOH solution. When the pH increased from 9 to 10, to 11, the shape of CoWO_4 product changed from truncated nanooctahedral nanocrystals to elongated nanocrystals ($\sim 40 \times 50 \text{ nm}$) and to nanorods ($\sim 40 \times 200 \text{ nm}$), respectively (Fig. 4b and c). The increase of pH in the reaction solution may influence the selective adsorption of the surfactant molecules on the growth surface of particles leading to the shape elongation of the products. For the MnWO_4 , ZnWO_4 , and CdWO_4 NC samples, the anisotropic morphologies of all

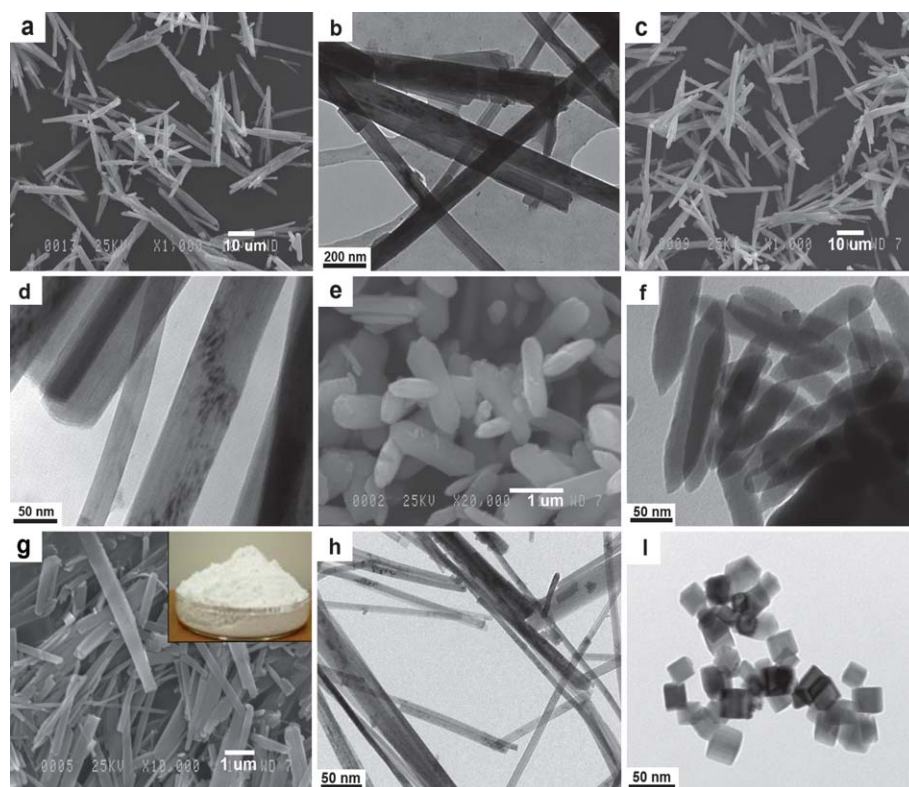


Fig. 2 SEM/TEM images of the metal oxide NC samples: (a and b) $80 \text{ nm} \times 6 \text{ } \mu\text{m}$ In_2O_3 nanorods, (b and c) $80 \text{ nm} \times 6 \text{ } \mu\text{m}$ Y_2O_3 nanorods, (d and e) $0.5 \text{ } \mu\text{m} \times 1 \text{ } \mu\text{m}$ ZrO_2 nanorods, (f and g) $60 \text{ nm} \times 8 \text{ } \mu\text{m}$ TiO_2 nanobelts, inset of (f), 31 g of the AHA-capped TiO_2 nanobelts obtained in a single preparation from 300 mL of the reaction solution using a 700 mL autoclave, and (h) 50 nm CeO_2 nanocubes.

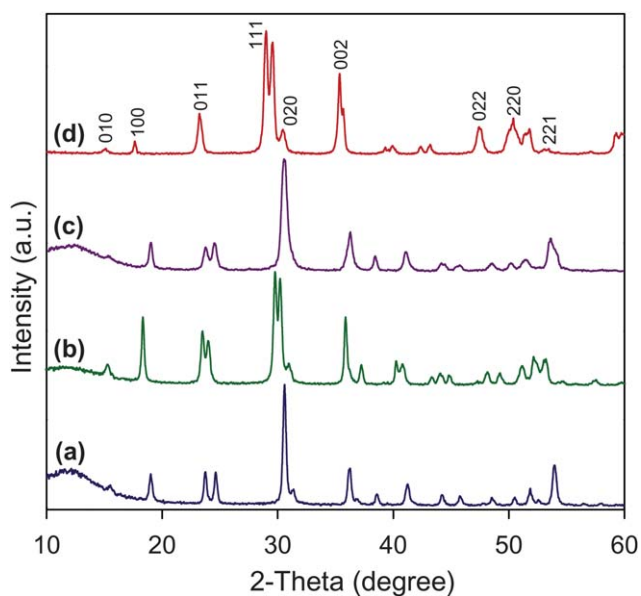


Fig. 3 XRD patterns of the as-synthesized transition metal tungstate NC samples: (a) CoWO_4 , (b) MnWO_4 , (c) ZnWO_4 , and (d) CdWO_4 .

products were found. The differences in the average aspect ratio (length/width namely as AAR) of the final NC products were observed: 25 nm \times 50 nm-sized MnWO_4 nanobars, AAR of 2.0 (Fig. 4f); 15 nm \times 70 nm-sized ZnWO_4 nanorods, AAR of 4.7

(Fig. 4h); 50 nm \times 160 nm-sized CdWO_4 nanorods, AAR of 3.2 (Fig. 4i), depending on the nature of transition metals. Interestingly, when the monomer precursor concentration decreases from 0.0150 to 0.0076 M in water medium, polypeptide-stabilized tungstate mesocrystal hierarchical microspheres (e.g., 3 μm -sized MnWO_4) were achieved. This could be due to the spontaneous-assembly of primary nanoparticles through the backbone-backbone intermolecular hydrogen-bonding interactions of polypeptide chains (Fig. 4g), as illustrated in our recent work.²⁴

For the rare earth orthovanadate NC samples (REVO_4 , RE = La, Ce, Nd, Sm, Gd, Er), XRD patterns of these samples are shown in Fig. 5. It is known that rare earth orthovanadates crystallize in two polymorphs including tetragonal phase (*t*-) and monoclinic phase (*m*-).³⁸ With an increase of ionic radius of rare earth (RE^{3+}), RE^{3+} ions show a strong tendency toward *m*-phase orthovanadate due to its higher oxygen coordination number; 9 compared to 8 of the *t*-phase orthovanadate. Because La^{3+} ion has the largest ionic radius in all rare earth ions, the thermodynamically stable state of *m*- LaVO_4 is much easier than the metastable state of *t*- LaVO_4 . In some cases, the tetragonal (*t*-) zircon type to monoclinic (*m*-) monazite type transformation often occurs at 850–900 °C or turns the pH value of synthesis solution.³⁹ In our present case, the monazite-type monoclinic LaVO_4 structure with cell parameters $a = 7.043 \text{ \AA}$, $b = 7.279 \text{ \AA}$, $c = 6.721 \text{ \AA}$ (JCPDS 50-0367) was formed (Fig. 5a). On the contrary, the XRD patterns of all other samples (Fig. 5b–f) show

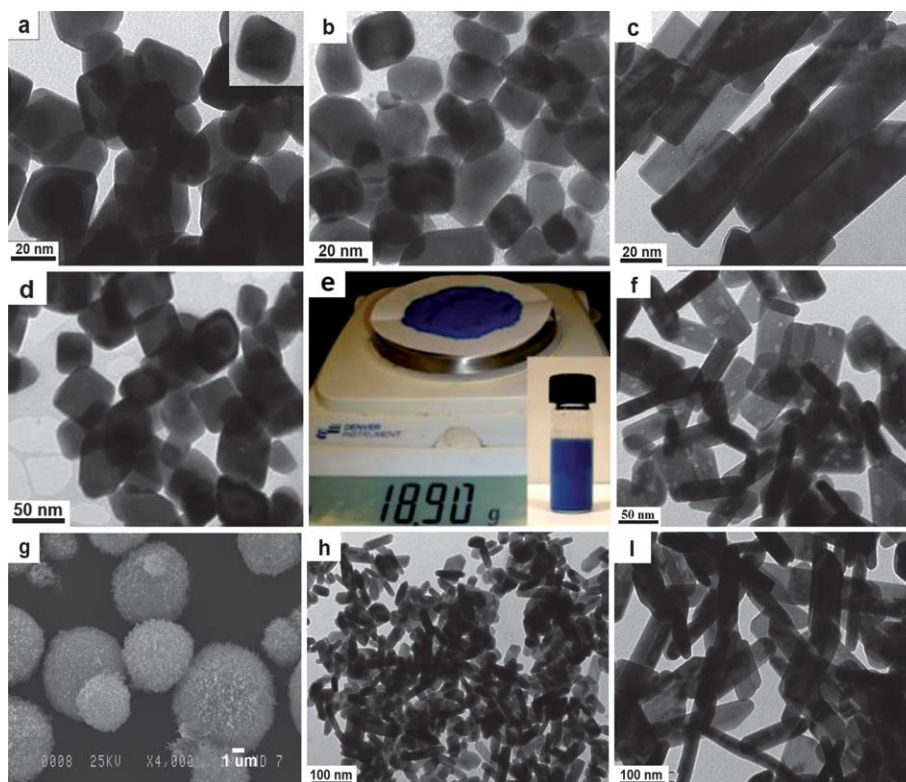


Fig. 4 TEM/SEM images of the transition-metal tungstate NC samples: CoWO_4 nanocrystals with various shapes of (a) truncated nanoctahedron, (b) nanobar, (c) nanorods, synthesized at different pH values of 9, 10, 11, respectively; (d) CoWO_4 truncated nanoctahedron synthesized in scale-up and (e) photograph of $\sim 18 \text{ g}$ of AHA-capped CoWO_4 truncated nanoctahedron obtained by a single run from 500 mL of the reaction solution using a 700 mL autoclave, inset of a vial of aqueous CoWO_4 NC suspension, (f) 25 nm \times 50 nm MnWO_4 nanobars, (g) 3 μm MnWO_4 microspheres, (h) 15 nm \times 70 nm ZnWO_4 nanorods, and (i) 50 nm \times 160 nm CdWO_4 nanorods.

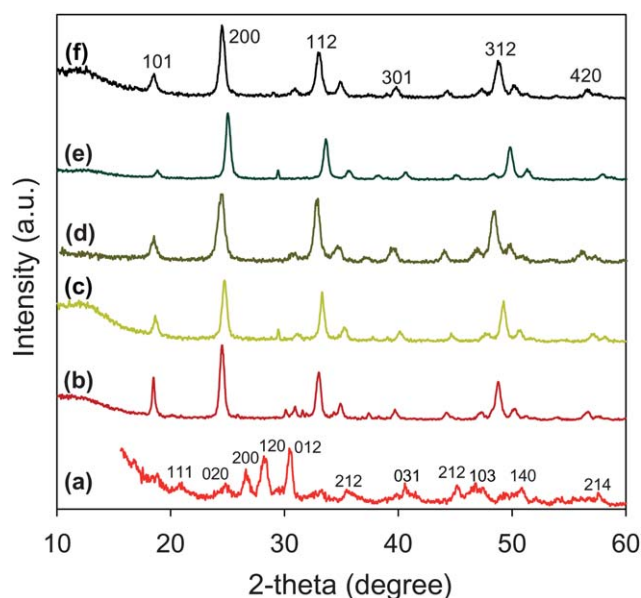


Fig. 5 XRD patterns of the as-synthesized rare earth orthovanadate NC samples: (a) LaVO_4 , (b) CeVO_4 , (c) NdVO_4 , (d) SmVO_4 , (e) GdVO_4 , and (f) ErVO_4 .

that all diffraction peaks of different products were well-indexed as pure tetragonal-zircon structure of REVO_4 ($\text{RE} = \text{Ce}, \text{Nd}, \text{Sm}, \text{Gd}, \text{Er}$). All the XRD patterns also show broad peaks due to their nanoscale size and no peaks of any other phases or impurities were detected.

As seen in Fig. 6, representative TEM images of these rare earth orthovanadate NCs (from panel a to l) exhibit two distinct shapes: rod for La, Ce, Nd, and ellipsoid/cube/sphere for Sm, Gd, Er. In Fig. 6a–c, TEM images of REVO_4 NCs ($\text{RE} = \text{La}, \text{Ce}, \text{Nd}$) clearly reveal a rod shape with an average size of 8 nm \times 40 nm for LaVO_4 ; 10 nm \times 30 nm for CeVO_4 ; and 10 nm \times 35 nm for NdVO_4 . However, TEM images in Fig. 6g–l exhibit ellipsoid for SmVO_4 , cube for GdVO_4 , and sphere for ErVO_4 with an average diameter of 30 nm. Further, the selected area electron diffraction (SAED) pattern (Fig. 6d) of the corresponding typical NdVO_4 sample is indexed to a monoclinic-phase single crystal, which is consistent with the above XRD data. Elemental dispersive spectrum (EDS) analysis (Fig. 6e) of the NdVO_4 sample determined the Nd : V molar ratios of 1 : 1. From a series of our present experiments, we found that under the same synthetic conditions, light rare earth orthovanadates ($\text{RE} = \text{La}, \text{Ce}, \text{Nd}$) readily form nanorods, whereas heavy rare earth orthovanadates ($\text{RE} = \text{Sm}, \text{Gd}, \text{Er}$) yield nanocubes/spheres. It seems that the shape of REVO_4 nanocrystals depends on ionic radius of rare earth. For the larger lanthanide ions (La, Ce, Nd), the corresponding orthovanadates exhibit rod shapes, whereas for the smaller ones (Sm, Gd, Er), the corresponding orthovanadates were found to be cube/sphere ones. Similar results for this type of rare earth vanadate materials were also reported by Li *et al.*⁴⁰

Rare earth doped orthovanadate nanocrystals have attracted great interest for their luminescent applications.^{41–43} In this work, Eu^{3+} doped NdVO_4 NCs as a typical example were synthesized using the similar method, and their optical properties were

studied. The doping Eu^{3+} ion in low concentration (5.0 mol% mol) would not have influence on shape of the NdVO_4 nanorods (Fig. 6f). Fig. S1† shows UV-visible adsorption, photoluminescent (PL) excitation and emission spectra of the as-prepared 5.0 mol% Eu^{3+} -doped NdVO_4 nanorods suspended in water. The UV region (Fig. S1a†) of this sample exhibits a strong absorption edge at ~ 283 nm attributing to the charge transfer from the oxygen ligands to the central vanadium atoms inside the VO_4^{3-} ions.⁴⁴ As shown in Fig. S1b†, under 218 nm excitation and emission, the excitation spectrum of this sample shows the excitation peaks (434 nm, ${}^7\text{F}_0\text{-}{}^5\text{L}_6$; 529 nm, ${}^7\text{F}_0\text{-}{}^5\text{D}_2$) of Eu^{3+} within its $4f^6$ configuration.^{44–46} The presence of the VO_4^{3-} absorption band in the excitation spectrum of Eu^{3+} reveals an energy transfer takes place from VO_4^{3-} to Eu^{3+} in the $\text{Eu}^{3+}:\text{NdVO}_4$.⁴⁷ The emission spectrum of this sample consists of the characteristic emission peaks (449 nm, ${}^5\text{D}_0\text{-}{}^7\text{F}_1$; 486 nm, ${}^5\text{D}_0\text{-}{}^7\text{F}_2$; 560 nm, ${}^5\text{D}_0\text{-}{}^7\text{F}_4$) of the f–f transition of Eu^{3+} , as reported previously for $\text{Eu}^{3+}:\text{YVO}_4$ nanocrystals.⁴¹

Furthermore, for the synthesis of rare earth molybdate NCs ($\text{RE}_2(\text{MoO}_4)_3$, $\text{RE} = \text{La}, \text{Ce}, \text{Gd}, \text{Y}, \text{Er}$), typical XRD patterns of these samples are shown in Fig. 7. The diffraction peaks of $\text{La}_2(\text{MoO}_4)_3$ sample were well-indexed to the tetragonal-phase structure with lattice parameters of $a = b = 5.343$ Å, $c = 11.780$ Å (JCPDS 45-0407). All the other $\text{RE}_2(\text{MoO}_4)_3$ ($\text{RE} = \text{Ce}, \text{Gd}, \text{Y}, \text{Er}$) were also well-indexed to the tetragonal-phase structure.⁴⁸ The XRD patterns also exhibit broad and intensive diffraction peaks due to their nanometre size and high crystallinity. The (112) peak is more intense than other reflection peaks, which implies the highly preferential oriented growth of the $\text{RE}_2(\text{MoO}_4)_3$ nanosheets, as seen in following SAED results. The morphologies of a series of $\text{RE}_2(\text{MoO}_4)_3$ nanocrystals were also examined by TEM/SEM images (Fig. 8a–f). TEM images of all samples, including $\text{La}_2(\text{MoO}_4)_3$, $\text{Ce}_2(\text{MoO}_4)_3$, $\text{Gd}_2(\text{MoO}_4)_3$, $\text{Y}_2(\text{MoO}_4)_3$, $\text{Er}_2(\text{MoO}_4)_3$ NCs, shared thin sheet shape, and their corner and edge were mostly broken or damaged. All the resulting nanosheets have an average side dimension of 200–300 nm and a thickness of ~ 2 nm. The SEM observation (inset) also indicates that almost 100% of the as-prepared products are super thin nanosheets and no other types of nanoparticles were found. Corresponding SAED patterns (inset of Fig. 8a–f) of all samples revealed the single-crystalline nature and indexed to tetragonal-phase $\text{RE}_2(\text{MoO}_4)_3$. The above results reveal that all the $\text{RE}_2(\text{MoO}_4)_3$ nanocrystals maintained the super-thin sheet morphology, and no significant influence of rare earth ionic radius on morphology of the products was observed. Further, the shape of $\text{RE}_2(\text{MoO}_4)_3$ nanocrystals was changed depending on reaction temperature (for the temperature less than 180 °C). Taking the $\text{La}_2(\text{MoO}_4)_3$ sample as a typical example, the synthesis was performed at 100, 130, 160 °C, the resulting products of $\text{La}_2(\text{MoO}_4)_3$ nanocrystals obtained with shapes of ~ 300 nm microspheres, ~ 110 nm \times 340 nm nanorods, ~ 2 nm \times 200–300 nm sheet-shaped nanosquares, respectively (Fig. 8g–l). These shape changes may close to minimize the surface energy of particle during the growth.

Similarly, as in the case of metal tungstate materials (Fig. 4g), these molybdate nanocrystals, for example, $\text{La}_2(\text{MoO}_4)_3$ could offer nanobuilding blocks for the further construction of the hierarchical aggregated microsphere materials, as seen in Fig. 8b. We expect that the 2D nanosheets and 3D assembled

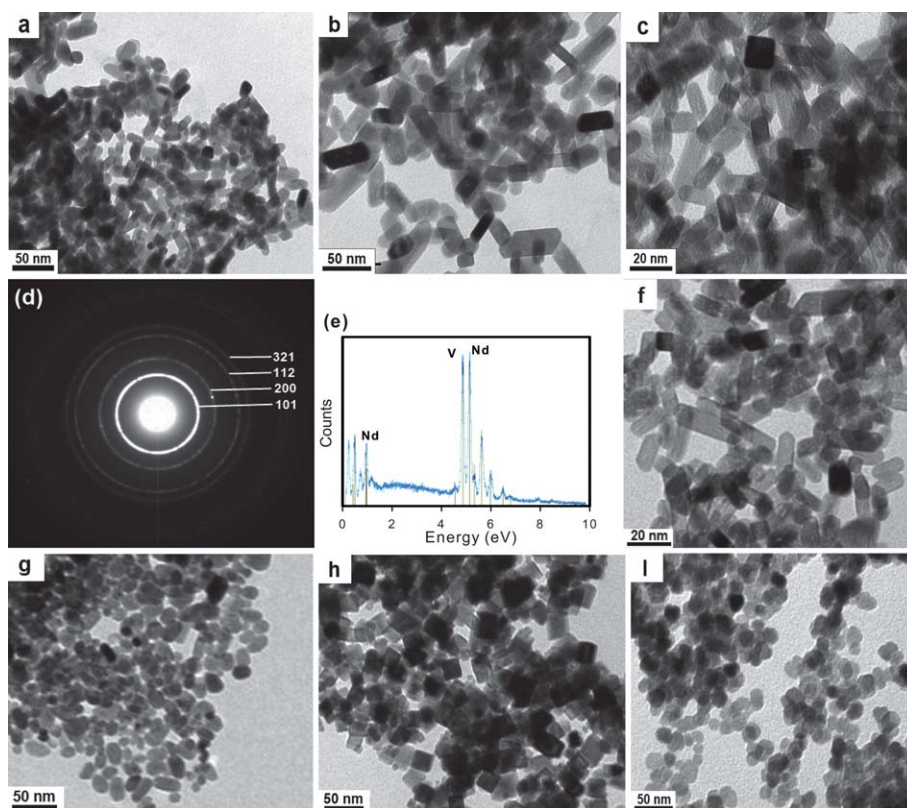


Fig. 6 TEM images of the rare earth orthovanadate NC samples: (a) 8 nm \times 40 nm LaVO_4 nanorods, (b) 10 nm \times 30 nm CeVO_4 nanorods, (c) 10 \times 35 nm NdVO_4 nanorods, (d) SAED and (e) EDS patterns of corresponding NdVO_4 , (f) 5.0 mol% $\text{Eu}^{3+}:\text{NdVO}_4$ nanorods, (g) 30 nm SmVO_4 nanoellipses, (h) 30 nm GdVO_4 nanocubes, and (i) 30 nm ErVO_4 nanospheres.

microspheres of rare earth molybdate materials have promising applications in electronic and optical fields, which mainly arise from their structural anisotropy, nearly perfect crystallinity, and quantum confinement effects in the thickness.⁴⁹ Furthermore,

such materials could act as a stable support for the preparation of doped nanomaterials, in particular, of nitrogen doped nanosheets to reduce the band-gap energy, which enhances their activity.⁵⁰

To understand the formation mechanism of the $\text{RE}_2(\text{MoO}_4)_3$ nanosheets, we systematically tracked the time course of the sheet growth process of a representative $\text{La}_2(\text{MoO}_4)_3$ sample. Fig. S2a–c† shows representative TEM images of the $\text{La}_2(\text{MoO}_4)_3$ samples synthesized at different reaction times, *e.g.*, 2, 6, and 20 h, while keeping the other experimental conditions unchanged (La/Mo of 2 : 3, AHA/(La + Mo) of 2 : 1, 180 °C). When the aging time reached 2 h, small particles tended to agglomerate together for the formation of the dense aggregates with size of ~ 200 nm (Fig. S2a†). A careful examination of the high-magnification TEM images (inset of Fig. S2a†) clearly indicates that all the aggregates are made up from small particles of ~ 2 nm. By further prolonging the reaction time to 6 h, these aggregates crystallized into the chains of irregular sheets, which were self-assembled into 2-D arrays (Fig. S2b†). Finally, when the reaction time is up to 20 h, these irregular species grew into the quite uniform nanosheets (Fig. S2c†).

On the basis of these TEM results, the transformation of dense aggregates of primary particles into $\text{RE}_2(\text{MoO}_4)_3$ nanosheets could be due to Ostwald ripening,⁵¹ lateral-aggregation,⁵² and dissolution/recrystallization⁵³ processes in the presence of 6-aminohexanoic acid molecules in water medium. The whole process is illustrated in Fig. S2d†. When two precursor solutions of La^{3+} cations and MoO_4^{2-} anions are mixed together in the

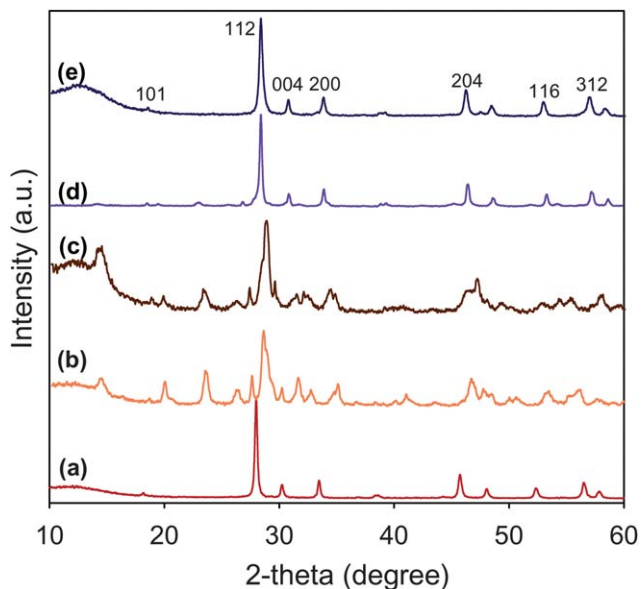


Fig. 7 XRD patterns of the as-synthesized rare earth molybdate NC samples: (a) $\text{La}_2(\text{MoO}_4)_3$, (b) $\text{Ce}_2(\text{MoO}_4)_3$, (c) $\text{Gd}_2(\text{MoO}_4)_3$, (d) $\text{Y}_2(\text{MoO}_4)_3$, and (e) $\text{Er}_2(\text{MoO}_4)_3$.

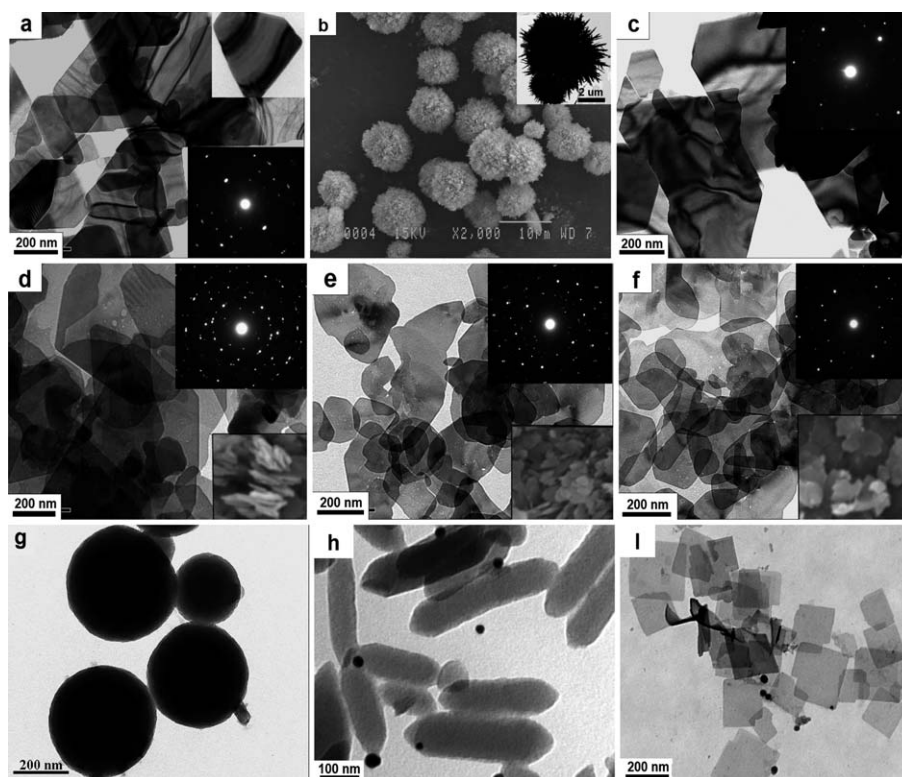


Fig. 8 TEM/SEM and inset SAED patterns of 2 nm \times 200–300 nm-sized rare earth molybdate nanosheets: (a) $\text{La}_2(\text{MoO}_4)_3$, (b) $\text{La}_2(\text{MoO}_4)_3$ microspheres, (c) $\text{Ce}_2(\text{MoO}_4)_3$, (d) $\text{Gd}_2(\text{MoO}_4)_3$, (e) $\text{Y}_2(\text{MoO}_4)_3$, and (f) $\text{Er}_2(\text{MoO}_4)_3$. Effect of reaction temperature on the shape of $\text{La}_2(\text{MoO}_4)_3$ crystals: (g) 100 °C, microspheres, (h) 130 °C, nanorods, and (i) 160 °C, sheet-shaped nanosquares.

presence of 6-aminohexanoic acid, an high supersaturating degree could be reached, and amorphous $\text{La}_2(\text{MoO}_4)_3$ particles were formed immediately. The tiny crystalline nuclei were firstly generated in a supersaturated solution at elevated temperature and then grew into nanoparticles by controlled crystallization and growth of the crystals through the process known as Ostwald ripening. Subsequently, the primary nanoparticles quickly build anisotropically and spontaneously self-aggregated along the 2D direction; the nanosheets were grown until all the particles were consumed through lateral-aggregation mechanism. Finally, the shape transformation of the crystallized nanosheets in the synthesis solution often operates through a classical dissolution–recrystallization mechanism to minimize the surface energy of the system, resulting in the formation of the quite uniform nanosheets.

Furthermore, to prove AHA capped on the surface of $\text{La}_2(\text{MoO}_4)_3$ nanosheets, two characterization techniques were used: XPS and FTIR. This sample was washed several times with distilled water, only ~ 2.0 atomic% of nitrogen from $-\text{NH}_2$ of 6-aminohexanoic acid molecules capped on the surface of $\text{La}_2(\text{MoO}_4)_3$ nanosheets was found by XPS technique, as shown in Fig. S3†. The O1s, C 1s, N 1s, C 1s XPS spectra (Fig. S3c and d†) of this sample suggest that 6-aminohexanoic acid molecules bound on the $\text{La}_2(\text{MoO}_4)_3$ NC surface. This result was further confirmed by FTIR spectrum. Fig. S4† shows that an IR band at 2900 cm^{-1} attributed to the C–H stretching vibrations of methylene groups of the AHA molecules were observed. Two bands at 1400 and 3460 cm^{-1} correspond to C–N bending and $-\text{NH}_2$ stretching modes of AHA molecules, respectively. This indicates

that the adsorption of $-\text{NH}_2$ groups on the oxide nanocrystal surface and free $-\text{COOH}$ groups was oriented outward, consequently the colloidal AHA-capped oxide nanocrystals became hydrophilic and dispersed in water medium, as previously illustrated by our group.²⁴ As compared to the nonaqueous synthetic routes using hydrophobic organic surfactants such as fatty acids, aliphatic amines, alkyl phosphine oxides, our aqueous medium-based approach has many advantages: water is adopted as the continuous solution phase and inorganic salts were used as starting materials; amphiphilic 6-aminohexanoic acid biomolecule is an interesting stabilizer to yield the biocompatible nanocrystal products. Because of the high solubility of the salts in aqueous solution, it could be applicable to synthesize the nanoparticles in scale up by using the high precursor monomer concentrations. It was found that the morphology of products was essentially unchanged with the use of large volume of the synthesis. For example, for TiO_2 and CoWO_4 NCs, we were able to prepare ultra-large quantities of 31 g of $60\text{ nm} \times 8\text{ }\mu\text{m}$ TiO_2 nanobelts (inset of Fig. 2g) and 18.9 g of 20 nm-sized CoWO_4 nano-octahedrons (inset of Fig. 4e) in a single run using a 700 mL-sized autoclave. The average yield of synthesis reaction was about 93% for metal oxides and 96% for mixed oxides (see Table 1). Hence, the current aqueous-based route is readily applicable to the large-scale synthesis for the academic laboratory as well as the industrial applications because of a simple way, simplicity, high yield, and the use of nontoxic cheap reagents.

Recently, noble-metal deposited semiconductor nanocrystals have been received much attention due to their unique photocatalytic performance.^{54,55} Our synthetic approach for such

noble-metal dispersed semiconductor NCs relies on two sequential seeded-growth steps, as sketched in Scheme 1C. Using the pre-synthesized AHA capped oxide nanocrystals as nano-support and metal nitrate as metal source, the amine group of AHA ligand was bonded to the surface of oxide nanocrystals and other end uncoordinated carboxylic acid of AHA was outwarded to water.²⁵ In water medium (pH \approx 7.5), noble-metal precursor cations strongly adsorbed on the negatively charged surface of 6-aminohexanoic acid-stabilized oxide nanocrystals through electrostatic attraction, due to the deprotonation of $-\text{COOH}$ groups (see Experimental section). This technique guarantees preferential heterogeneous nucleation and growth metal precursors on the surface of the substrate seeds *via* the interaction between noble-metal precursor and uncoordinated carboxylic group of AHA-capped oxide nanocrystals followed by reduction using NaBH_4 . This leads to the high dispersion of tiny metal particles on the nanosupport. Here we selected four metal oxide NCs: CeO_2 , TiO_2 , In_2O_3 , Y_2O_3 and three mixed oxide NCs: CoWO_4 , MnWO_4 , $\text{La}_2(\text{MoO}_4)_3$, and two noble metals: Ag, Au, as typical examples for the syntheses of metal–semiconductor nanohybrids. Nanohybrids of Ag/CeO_2 , $\text{Ag}/\text{Y}_2\text{O}_3$, $\text{Ag}/\text{In}_2\text{O}_3$, Ag/MnWO_4 , Au/MnWO_4 , Ag/CoWO_4 , Au/CoWO_4 , $\text{Au}/\text{La}_2(\text{MoO}_4)_3$ were successfully prepared. The whole loading amount of metal was kept to 10.0 weight percent. The structural-compositional details of the heterostructures have been studied by multi-technique combination including TEM, XRD, XPS, UV-vis analyses.

TEM images of a variety of metal/oxide nanohybrids with a noble-metal content of 10.0 wt% show that such nanohybrids

consisted of metallic clusters/dots and oxide NC supports, as presented in Fig. 9. Also, one can see that numerous deposited metallic nanoparticles were attached to a oxide nanocrystal support. The 5–7 nm-sized Ag nanodots were observed, while the tiny Au nanodots with smaller diameter of 2–3 nm were dispersed effectively on the hydrophilic surface of support. Metal aggregates were also not found by the TEM observation. In all cases, after decorating with a metallic ion precursor, tiny Ag or Au nanodots formed and grew on the surface and the surfaces become coarse. It was noteworthy that no separated noble-metal particles were observed, indicating that the AHA-stabilized oxide nanocrystals provide a large number of adsorption sites for the noble metal nucleated and grown on the oxide NC surface under our experimental conditions. The resulting metal nanoclusters/dots thus are evenly distributed over the entire NC surface without significant overlap. For the metal (Ag, Au)/oxide hybrid samples, XRD spectra (Fig. S5 and S6 in ESI[†]) exhibited two sets of strong diffraction peaks, indicating that the hybrid products are composite materials with high crystallinity. Those marked with “*” can be indexed to face-centered cubic (fcc) Ag structure (JCPDS 74-1728),⁵⁶ and face-centered cubic (fcc) Au structure (JCPDS 01-1174),⁵⁷ while the others can be indexed to the corresponding oxide structure.

The particle size dependence of the electronic properties has been reported in the literature.^{30,58,59} In this work, the Ag/TiO_2 nanobelt sample was selected as a typical example. In this case, the size of Ag particles and their distribution on the TiO_2 nanobelt surface were conducted by tuning the silver precursor

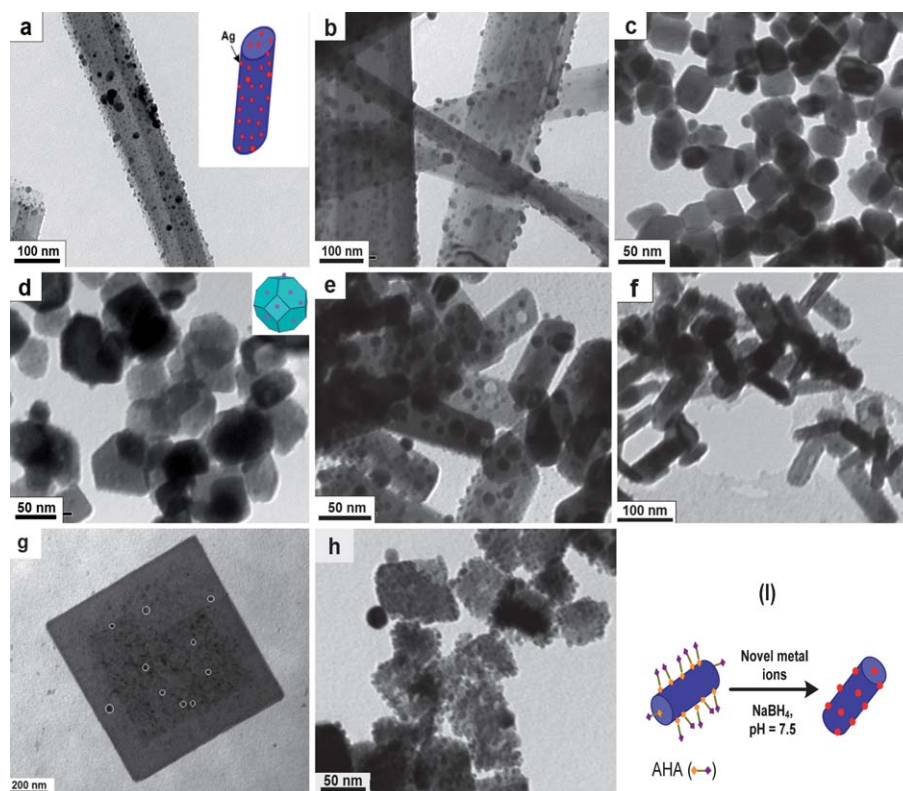


Fig. 9 TEM images of 10.0 wt% noble-metal/oxide nanohybrid samples: (a) $\text{Ag}/\text{In}_2\text{O}_3$, (b) $\text{Ag}/\text{Y}_2\text{O}_3$, (c) Ag/CoWO_4 , (d) Au/CoWO_4 , (e) Ag/MnWO_4 , (f) Au/MnWO_4 , (g) $\text{Au}/\text{La}_2(\text{MoO}_4)_3$, (h) Ag/CeO_2 , and (i) scheme of the proposed mechanism of metal precursors deposited on the pre-synthesized oxide nanocrystals for the formation of metal/oxide nanohybrids.

concentrations in the synthesis solution. Fig. 10 shows TEM images of hybrid Ag/TiO₂ nanobelts prepared with different Ag contents ranging from 5.0 to 10.0 and 15.0 wt% in the synthesis solution. The Ag concentration in solid solution was determined by XPS technique. The Ag amount in 5.0 wt% Ag/TiO₂, 10.0 wt% Ag/TiO₂, 15.0 wt% Ag/TiO₂ samples was estimated to be 4.8, 9.5, 14.6 wt%, respectively, corresponding to 4.8 wt% Ag/TiO₂, 9.5 wt% Ag/TiO₂, 14.6 wt% Ag/TiO₂. When 4.8 wt% Ag was deposited on TiO₂ nanobelts, very small Ag nanoclusters with an average diameter of ~2 to 3 nm were observed (Fig. 10a). When the Ag loading was increased to 9.5 wt% Ag nanodots with a particle size of 5–7 nm was found (Fig. 10b). In both cases, they were highly dispersed on the nanobelt surface. No evidence of Ag aggregates was detected. With higher Ag loading (14.6 wt%), the Ag particles with a larger size (15–20 nm) and a broad distribution were found (Fig. 10c). Further increasing this ratio (e.g., >14.6 wt%), large Ag particles and only few smaller particles were observed, indicating that a coalescence of Ag particles occurred during the synthesis. The crystalline feature of the as-prepared nanohybrids was also confirmed by dark-field TEM analysis (Fig. 10d). Using this approach, a high dispersion of Ag nanoparticles can be obtained, and their size can be tuned by Ag concentration in the synthesis solution.

The as-prepared 9.5 wt% Ag/TiO₂ nanobelt sample was characterized by XPS technique for the evaluation of the metal oxidation state. Fig. S7† displays high-resolution XPS spectra for Ti 2p and Ag 3d species. The Ti 2p spectrum (Fig. S7a†) exhibits two peaks. The Ti 2p_{3/2} and Ti 2p_{1/2} peaks are centered at 450.3 and 456.1 eV, respectively, with $\Delta \approx 5.8$ eV, indicating those of pure TiO₂ phase.⁶⁰ The Ag 3d_{5/2} peak (Fig. S7b†) is centered at 367.7 eV, which are attributed to metallic Ag.⁶¹ Remarkably, this Ag 3d_{5/2} binding energy value of the Ag/TiO₂ sample is lower as compared to that of the pure metallic Ag (368.0 eV). Furthermore, as seen in Fig. S8†, O 1s XPS spectrum

exhibits two peaks: one peak at 528.8 eV corresponds to oxygen in the lattice of TiO₂ NCs and the other one at 530.7 eV can be attributed to the adsorbed oxygen on the TiO₂ NC surface. The results indicate that the shift of the binding energy of Ag 3d_{5/2} to the lower site can be mainly ascribed to the electrostatic interaction between the deposited Ag clusters and TiO₂ nanobelts.

UV-visible spectra of the synthesized Ag/TiO₂ samples with Ag loadings of 4.8, 9.5, 14.6 wt% are shown in Fig. 11. For pure TiO₂ nanobelts, the optical absorption threshold peak is located approximately at 280–290 nm which corresponds to the band gap energy value of 3.18 eV.⁶² This value is very close to that of the commercial TiO₂ (Degussa P-25, $E_g = 3.2$ eV).⁶³ For the Ag/TiO₂ nanobelts with different Ag loadings, an additional peak at 352 nm was observed. This peak is attributable to the metallic Ag nanodots on the Ag/TiO₂ heterostructures.⁵⁶ The intensity of this peak increases as a function of Ag loading in the Ag/TiO₂ sample. Its intensity increases gradually with an increase of the Ag content from 4.8 to 14.6 wt%, possibly due to the size-dependent surface plasmon resonance effect of metallic Ag clusters and the interaction between Ag clusters and TiO₂ NCs.

The metal–semiconductor nanohybrids are expected to exhibit high photocatalytic efficiency. To evaluate the photocatalytic performance, we selected the 9.5 wt% Ag/TiO₂ sample for the photocatalytic decomposition of methylene blue (MB) in water under UV illumination. The 9.5 wt% Ag/TiO₂ hybrid nanobelt sample after calcination at 500 °C at 2 h possesses surface area of 32 m² g⁻¹ and pore volume of 0.42 cm³ g⁻¹ (Fig. S9†). In comparison, the samples of pure TiO₂ nanobelts, commercial TiO₂-P25, 9.5 wt% Ag/TiO₂ nanohybrids and 9.5 wt% Ag/TiO₂-P25 were used under the same testing conditions. As seen in Fig. S10A†, UV-visible spectra of the MB aqueous solution (16 mL, 0.05 mM) containing 0.015 g catalysts were recorded at different time intervals. The absorption double peaks at 609 and 667 nm are characteristic of methylene blue. The intensity of these peaks decreases as a function of irradiation time, indicating the decomposition of MB. For the 9.5 wt% Ag/TiO₂ hybrid catalyst, after 80 min of reaction time, these peaks completely disappeared, indicating the complete degradation of methylene

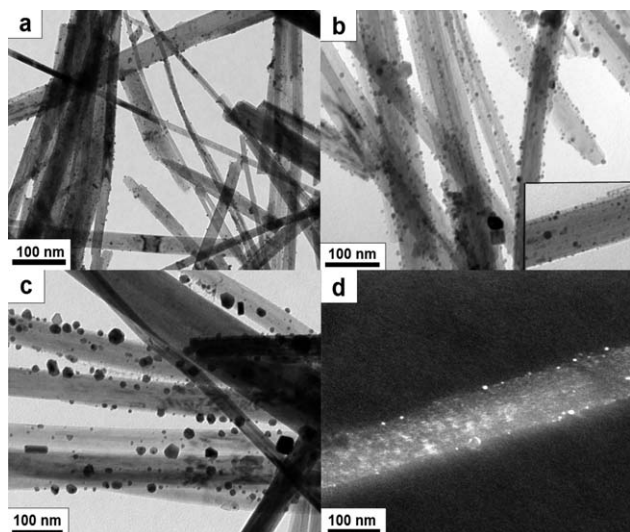


Fig. 10 Effect of Ag ion content (C , wt%) on Ag particle diameters (d) in the solid solution. TEM images of the Ag/TiO₂ hybrid nanobelt samples with different Ag contents (C , wt%): (a) $C = 4.8$, $d = 2\text{--}3$ nm (b) $C = 9.5$, $d = 5\text{--}7$ nm, (c) $C = 14.6$, $d = 15\text{--}20$ nm, (d) dark-field TEM image of a single 9.5 wt% Ag/TiO₂ nanobelt.

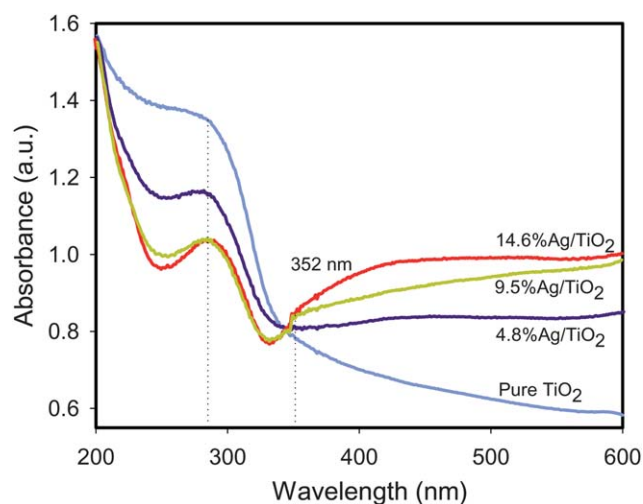


Fig. 11 UV-visible absorption spectra of the as-synthesized Ag/TiO₂ nanohybrids with the different Ag contents.

blue in the aqueous solution. The pure TiO₂ nanobelts show a slightly higher catalytic activity than that of commercial TiO₂-P25. This could be due to the shape effect on the photocatalytic efficiency (Fig. S10B†). Both hybrid Ag/TiO₂ materials show better photocatalytic activity than that of pure TiO₂ materials. However, the hybrid Ag/TiO₂ nanobelts clearly exhibit a much higher performance for the photocatalytic degradation of MB as compared to Ag/P25. The high photocatalytic activity of Ag/TiO₂ NCs could be due to a very high dispersion of Ag clusters on the individual TiO₂ NCs and the TiO₂ shape effect.

A possible photocatalytic mechanism of Ag/TiO₂ system is proposed in Scheme S1†. In the Ag–TiO₂ system, electrons will migrate from Ag to the conduction band (CB) of TiO₂ to achieve the Fermi level equilibration through Ag–TiO₂ interaction. When the catalysts are illuminated by UV light with photon energy higher than the band gap of TiO₂, electrons (e⁻) in the valence band (VB) can be excited to the CB with simultaneous generation of the same amount of holes (h⁺) left behind. The deflected energy band in the space charge region facilitates the rapid transfer of the as-excited electrons from TiO₂ to Ag nanoparticles, which increases the lifetime of the photogenerated pairs. Electrons accumulated at Ag particles or the conduction band of TiO₂ can be transferred to oxygen molecules adsorbed on the surface to form free oxygen radicals, such as [•]O₂⁻, [•]HO₂, [•]OH, while the photoinduced holes are apt to react with surface-bound H₂O or OH⁻ to produce the hydroxyl radical species ([•]OH) which is an extremely strong oxidant for the mineralization of organic chemicals (e.g., MB).

4. Conclusion

In summary, we have demonstrated a general method for the hydrothermal high-yield synthesis of many kinds of the highly crystalline metal oxide (e.g., In₂O₃, Y₂O₃, ZrO₂, CeO₂) and mixed oxide nanocrystals (MWO₄, REVO₄, RE₂(MoO₄)₃, M = Co, Mn, Cd, Zn; RE = La, Ce, Gd, Nd, Y, Er) with various morphologies including belt, rod, truncated-octahedron, cubic, sphere and sheet. The synthetic procedure was based on the hydrothermal crystallization of inorganic precursors in water medium in the presence of bifunctional 6-aminohexanoic acid (AHA) as a capping agent. The resultant AHA-capped nanocrystals are suspended in water medium due to their hydrophilic surface character. The shape of some nanocrystals (e.g., CoWO₄, La₂(MoO₄)₃) can be controlled by simply adjusting the synthesis conditions such as pH of the solution and reaction temperature. Further at low precursor monomer concentration (e.g., 0.0075 M) in synthetic water solution, the mesocrystal hierarchical aggregated microspheres of MnWO₄ and La₂(MoO₄)₃ obtained from the spontaneous assembly of individual AHA-capped nanoparticles. This synthesis method is simple, inexpensive (metal salts instead of metal alkoxides as starting metal sources in water medium), and easy to scale-up to multigram-scale products (e.g., ~31 g of AHA-capped TiO₂ nanobelts and ~18 g AHA-capped CoWO₄ nanooctahedrons per a single preparation).

These AHA-capped oxide nanocrystals are excellent support for the preparation of a variety of metal/oxide hybrid nanocrystals, in which noble metal (Ag, Au) particles with the average size of 2–7 nm were deposited on the hydrophilic surface of

individual supports. We have demonstrated that hybrid Ag/TiO₂ nanobelts show a much higher performance for the photocatalytic degradation of MB as compared to Ag/commercial P25. Such hybrid metal/oxide nanomaterials have potential applications in many fields, such as environmental clean-up, optical coating, photovoltaic cells, gas sensors, optoelectronic, and so on. The present study on such metal/oxide nanohybrids motivates us to further explore other promising applications such as optical coating, photovoltaic cells, gas sensors, optoelectronic devices, and so on.

Acknowledgements

This work was supported by the Natural Sciences and Engineering Research Council of Canada (NSERC) through a strategic grant.

References

- 1 M. Fernández-García, et al., Nanostructured oxides in chemistry: characterization and properties, *Chem. Rev.*, 2004, **104**(9), 4063–4104.
- 2 R. Ferrando, J. Jellinek and R. L. Johnston, Nanoalloys: from theory to applications of alloy clusters and nanoparticles, *Chem. Rev.*, 2008, **108**(3), 845–910.
- 3 D. V. Talapin, et al., Prospects of colloidal nanocrystals for electronic and optoelectronic applications, *Chem. Rev.*, 2009, **110**(1), 389–458.
- 4 A. F. Taylor, et al., Dynamical quorum sensing and synchronization in large populations of chemical oscillators, *Science*, 2009, **323**(5914), 614–617.
- 5 Y. Xie, et al., *In situ* controllable loading of ultrafine noble metal particles on titania, *J. Am. Chem. Soc.*, 2009, **131**(19), 6648–6649.
- 6 M. Jakob, H. Levanon and P. V. Kamat, Charge distribution between UV-irradiated TiO₂ and gold nanoparticles: determination of shift in the Fermi level, *Nano Lett.*, 2003, **3**(3), 353–358.
- 7 V. Subramanian, E. E. Wolf and P. V. Kamat, Green emission to probe photoinduced charging events in ZnO–Au nanoparticles. Charge distribution and Fermi-level equilibration, *J. Phys. Chem. B*, 2003, **107**(30), 7479–7485.
- 8 S. Chakraborty, et al., Asymmetric dumbbells from selective deposition of metals on seeded semiconductor nanorods, *Angew. Chem., Int. Ed.*, 2010, **49**(16), 2888–2892.
- 9 S. G. Kwon and T. Hyeon, Colloidal chemical synthesis and formation kinetics of uniformly sized nanocrystals of metals, oxides, and chalcogenides, *Acc. Chem. Res.*, 2008, **41**(12), 1696–1709.
- 10 M. Niederberger, Nonaqueous sol–gel routes to metal oxide nanoparticles, *Acc. Chem. Res.*, 2007, **40**(9), 793–800.
- 11 X. Wang, et al., A general strategy for nanocrystal synthesis, *Nature*, 2005, **437**(7055), 121–124.
- 12 J. Yang, E. Sargent, S. Kelley and J. Y. Ying, A general phase-transfer protocol for metal ions and its application in nanocrystal synthesis, *Nat. Mater.*, 2009, **8**(8), 683–689.
- 13 T.-D. Nguyen and T.-O. Do, General two-phase routes to synthesize colloidal metal oxide nanocrystals: simple synthesis and ordered self-assembly structures, *J. Phys. Chem. C*, 2009, **113**(26), 11204–11214.
- 14 T. D. Nguyen, C. T. Dinh and T. O. Do, Two-phase synthesis of colloidal annular-shaped Ce_xLa_{1-x}CO₃OH nanoarchitectures assembled from small particles and their thermal conversion to derived mixed oxides, *Inorg. Chem.*, 2011, **50**(4), 1309–1320.
- 15 T.-D. Nguyen and T.-O. Do, Solvo-hydrothermal approach for the shape-selective synthesis of vanadium oxide nanocrystals and their characterization, *Langmuir*, 2009, **25**(9), 5322–5332.
- 16 T.-D. Nguyen, et al., A novel approach for monodisperse samarium orthovanadate nanocrystals: controlled synthesis and characterization, *J. Phys. Chem. C*, 2009, **113**(43), 18584–18595.
- 17 T.-D. Nguyen, C.-T. Dinh and T.-O. Do, Monodisperse samarium and cerium orthovanadate nanocrystals and metal oxidation states on the nanocrystal surface, *Langmuir*, 2009, **25**(18), 11142–11148.
- 18 Y.-w. Jun, J.-s. Choi and J. Cheon, Shape control of semiconductor and metal oxide nanocrystals through nonhydrolytic colloidal routes, *Angew. Chem., Int. Ed.*, 2006, **45**(21), 3414–3439.

- 19 F. C. Meldrum and H. Cölfen, Controlling mineral morphologies and structures in biological and synthetic systems, *Chem. Rev.*, 2008, **108**(11), 4332–4432.
- 20 P. Lakshminarayana and X. Qing-Hua, A single-step synthesis of gold nanochains using an amino acid as a capping agent and characterization of their optical properties, *Nanotechnology*, 2008, **19**(7), 075601.
- 21 T. Serizawa, Y. Hirai and M. Aizawa, Novel synthetic route to peptide-capped gold nanoparticles, *Langmuir*, 2009, **25**(20), 12229–12234.
- 22 C.-T. Dinh, et al., Shape-controlled synthesis of highly crystalline titania nanocrystals, *ACS Nano*, 2009, **3**(11), 3737–3743.
- 23 T.-D. Nguyen, C.-T. Dinh and T.-O. Do, Shape- and size-controlled synthesis of monoclinic ErOOH and cubic Er₂O₃ from micro- to nanostructures and their upconversion luminescence, *ACS Nano*, 2010, **4**(4), 2263–2273.
- 24 T.-D. Nguyen, et al., Biomolecule-assisted route for shape-controlled synthesis of single-crystalline MnWO₄ nanoparticles and spontaneous assembly of polypeptide-stabilized mesocrystal microspheres, *CrystEngComm*, 2011, **13**, 1450–1460.
- 25 M. R. Hoffmann, et al., Environmental applications of semiconductor photocatalysis, *Chem. Rev.*, 1995, **95**(1), 69–96.
- 26 A. M. Smith and S. Nie, Semiconductor nanocrystals: structure, properties, and band gap engineering, *Acc. Chem. Res.*, 2009, **43**(2), 190–200.
- 27 A. Corma, P. Serna and H. García, Gold catalysts open a new general chemoselective route to synthesize oximes by hydrogenation of α,β -unsaturated nitrocompounds with H₂, *J. Am. Chem. Soc.*, 2007, **129**(20), 6358–6359.
- 28 M. Chen and D. W. Goodman, Catalytically active gold: from nanoparticles to ultrathin films, *Acc. Chem. Res.*, 2006, **39**(10), 739–746.
- 29 Y. Sun, et al., Carbon-in-Al₄C₃ nanowire superstructures for field emitters, *ACS Nano*, 2011.
- 30 G. Menagen, et al., Au growth on semiconductor nanorods: photoinduced versus thermal growth mechanisms, *J. Am. Chem. Soc.*, 2009, **131**(47), 17406–17411.
- 31 L. Feng, et al., Well-controlled synthesis of Au@Pt nanostructures by gold-nanorod-seeded growth, *Chem.–Eur. J.*, 2008, **14**(31), 9764–9771.
- 32 S.-H. Yu, et al., Synthesis of very thin 1D and 2D CdWO₄ nanoparticles with improved fluorescence behavior by polymer-controlled crystallization, *Angew. Chem.*, 2002, **114**(13), 2462–2466.
- 33 C. Santato, et al., Crystallographically oriented mesoporous WO₃ films: synthesis, characterization, and applications, *J. Am. Chem. Soc.*, 2001, **123**(43), 10639–10649.
- 34 E. Rossinyol, et al., Synthesis and characterization of chromium-doped mesoporous tungsten oxide for gas sensing applications, *Adv. Funct. Mater.*, 2007, **17**(11), 1801–1806.
- 35 L. Zhang, et al., Bi₂WO₆ nano- and microstructures: shape control and associated visible-light-driven photocatalytic activities, *Small*, 2007, **3**(9), 1618–1625.
- 36 S. B. Stevens, et al., NaLa(MoO₄)₂ as a laser host material, *Phys. Rev. B: Condens. Matter*, 1991, **43**(10), 7386.
- 37 E. Downing, et al., A three-color, solid-state, three-dimensional display, *Science*, 1996, **273**(5279), 1185–1189.
- 38 W. Fan, et al., Selected-control hydrothermal synthesis and formation mechanism of monazite- and zircon-type LaVO₄ nanocrystals, *J. Phys. Chem. B*, 2006, **110**(46), 23247–23254.
- 39 C.-J. Jia, et al., Selective synthesis of monazite- and zircon-type LaVO₄ nanocrystals, *J. Phys. Chem. B*, 2005, **109**(8), 3284–3290.
- 40 X. Wang, et al., Hydrothermal synthesis of rare-earth fluoride nanocrystals, *Inorg. Chem.*, 2006, **45**(17), 6661–6665.
- 41 G. Wang, et al., Enhanced photoluminescence of water soluble YVO₄:Ln³⁺ (Ln = Eu, Dy, Sm, and Ce) nanocrystals by Ba²⁺ doping, *J. Phys. Chem. C*, 2008, **112**(44), 17042–17045.
- 42 G. Mialon, et al., New insights into size effects in luminescent oxide nanocrystals, *J. Phys. Chem. C*, 2009, **113**(43), 18699–18706.
- 43 E. Antic-Fidancev, et al., Simulation of the energy level scheme of Nd³⁺ and Eu³⁺ ions in rare-earth orthovanadates and phosphates, *J. Phys.: Condens. Matter*, 1991, **3**(35), 6829.
- 44 J. Liu and Y. Li, General synthesis of colloidal rare earth orthovanadate nanocrystals, *J. Mater. Chem.*, 2007, **17**(18), 1797–1803.
- 45 X. Wu, et al., Preparation of single-crystalline NdVO₄ nanorods, and their emissions in the ultraviolet and blue under ultraviolet excitation, *J. Phys. Chem. B*, 2005, **109**(23), 11544–11547.
- 46 S. Jandl, et al., Raman active phonon and crystal-field studies of Yb³⁺ doped NdVO₄, *Opt. Mater.*, 2010, **32**(11), 1549–1552.
- 47 C. Yu, et al., Spindle-like lanthanide orthovanadate nanoparticles: facile synthesis by ultrasonic irradiation, characterization, and luminescent properties, *Cryst. Growth Des.*, 2008, **9**(2), 783–791.
- 48 W. Bu, et al., Controlled construction of uniform pompon-shaped microarchitectures self-assembled from single-crystalline lanthanum molybdate nanoflakes, *Langmuir*, 2007, **23**(17), 9002–9007.
- 49 R. Ma and T. Sasaki, Nanosheets of oxides and hydroxides: ultimate 2D charge-bearing functional crystallites, *Adv. Mater.*, 2010, **22**(45), 5082–5104.
- 50 Y. Matsumoto, et al., N doping of oxide nanosheets, *J. Am. Chem. Soc.*, 2009, **131**(19), 6644–6645.
- 51 J. Tang and A. P. Alivisatos, Crystal splitting in the growth of Bi₂S₃, *Nano Lett.*, 2006, **6**(12), 2701–2706.
- 52 T.-D. Nguyen, D. Mrabet and T.-O. Do, Controlled self-assembly of Sm₂O₃ nanoparticles into nanorods: simple and large scale synthesis using bulk Sm₂O₃ powders, *J. Phys. Chem. C*, 2008, **112**(39), 15226–15235.
- 53 Z. Luo, et al., Synthesis of BaMoO₄ nestlike nanostructures under a new growth mechanism, *Cryst. Growth Des.*, 2008, **8**(7), 2275–2281.
- 54 R. Costi, A. E. Saunders and U. Banin, Colloidal hybrid nanostructures: a new type of functional materials, *Angew. Chem., Int. Ed.*, 2010, **49**(29), 4878–4897.
- 55 P. D. Cozzoli and L. Manna, Asymmetric nanoparticles: tips on growing nanocrystals, *Nat. Mater.*, 2005, **4**(11), 801–802.
- 56 M. Chen, et al., Silver nanoparticles capped by oleylamine: formation, growth, and self-organization, *Langmuir*, 2007, **23**(10), 5296–5304.
- 57 X.-F. Wu, et al., Synthesis of core-shell Au@TiO₂ nanoparticles with truncated wedge-shaped morphology and their photocatalytic properties, *Langmuir*, 2009, **25**(11), 6438–6447.
- 58 J. E. Macdonald, et al., Hybrid nanoscale inorganic cages, *Nat. Mater.*, 2010, **9**(10), 810–815.
- 59 R. Costi, et al., Electrostatic force microscopy study of single Au–CdSe hybrid nanodumbbells: evidence for light-induced charge separation, *Nano Lett.*, 2009, **9**(5), 2031–2039.
- 60 X. Chen and C. Burda, The electronic origin of the visible-light absorption properties of C-, N- and S-doped TiO₂ nanomaterials, *J. Am. Chem. Soc.*, 2008, **130**(15), 5018–5019.
- 61 N. R. Sieb, et al., Hollow metal nanorods with tunable dimensions, porosity, and photonic properties, *ACS Nano*, 2009, **3**(6), 1365–1372.
- 62 M. N. Tahir, et al., Facile synthesis and characterization of functionalized, monocrystalline rutile TiO₂ nanorods, *Langmuir*, 2006, **22**(12), 5209–5212.
- 63 K. Nagaveni, et al., Solar photocatalytic degradation of dyes: high activity of combustion synthesized nano TiO₂, *Appl. Catal., B*, 2004, **48**(2), 83–93.